Improving the Mathematical Formulas for Identification of Bitumen's Viscoelastic Properties at Large Shear Strains

Magnus Komperød[1]

[1]Technological Analyses Centre, Nexans Norway AS, Norway, magnus.komperod@nexans.com

Abstract

Bitumen is used as anticorrosion to protect steel armor wires of subsea cables and umbilicals. Because bitumen's viscoelastic behavior influences the mechanical properties of cables, it is desirable to include bitumen in mechanical cable analyses. For this purpose, the author and his colleagues have in a previous scientific paper presented a newly developed laboratory instrument for identification of bitumen's viscoelastic properties. The present paper derives an improved mathematical model for how to establish bitumen's viscoelastic properties from the sensor measurements of the laboratory instrument. It is proved mathematically that the model of the previous paper and the model of the present paper give identical results when bitumen has shear modulus of small magnitude. The difference between the two models grows with increasing magnitude.

Keywords: Arctic Engineering; Bitumen; Complex Analysis; Cross Section Analysis; Large Shear Strain; Offshore Technology; Subsea Cable; Umbilical.

1 Introduction

Subsea power cables are essential for connecting power grids across seas, such as connecting the Scandinavian Peninsula, i.e. Norway and Sweden, to Finland and the Baltic countries in east, to Denmark and Germany in south, and to Britain in southwest.

For offshore oil and gas production, umbilicals are most important. Umbilicals are cable-like structures consisting of different types of elements, such as tubes for transportation of fluids and for running hydraulic equipment, as well as electric and fiber optic signal cables. Power umbilicals also include power phases for energizing subsea equipment, such as subsea compressors.

Both subsea cables and umbilicals often include helical armor wires, usually arranged in one to four armor layers located outside the other cable elements. The main purpose of the armor wires is to carry axial tension and thereby reduce the axial tension imposed on the other cable elements. Armor wires may also be used to tune the cables' and umbilicals' submerged-weight-to-diameter ratio, where the submerged weight is the net force of gravity minus buoyancy. Figure 1 shows a subsea power cable with two layers of armor wires.

Figure 1. Subsea power cable. The two black arrows indicate the two layers of galvanized steel armor wires.

Armor wires are often made of galvanized steel, because this material has favorable mechanical properties, while being cost effective. However, as the cable is constantly submerged in seawater for decades, the galvanization may be insufficient corrosion protection for the steel wires. The viscoelastic material bitumen is commonly used as corrosion protection for the steel armor wires.

Olsen et al. (2014), Konradsen and Ouren (2014), Mullins et al. (2015), and Komperød et al. (2015) present efforts within identification of bitumen's viscoelastic properties for the purpose of including bitumen's behavior in cable analyses. Hedlund (2015) derives a model which describes how bitumen-coated armor wires influence the bending characteristics of subsea cables. A cable's bending characteristic describes the relationship between bending moment and bending curvature, which can be either static or dynamic. The model of Hedlund (2015) is based on the work of Mullins et al. (2015).

For many structures, for example steel tubes, the bending moment and the bending curvature are related through a real (non-complex) coefficient of proportionality, which is referred to as the structure's bending stiffness. However, for cables and umbilicals the bending characteristics may be nonlinear due to nonlinear materials, such as lead sheaths on power phases, and due to stick / slip behavior of helical elements as explained in Féret and Bournazel (1987) and in Caire (2014). Further, the bending characteristics may include dynamic behaviors due to viscoelastic materials, which is the case for cables and umbilicals with bitumen-coated armor wires.

The efforts of Olsen et al. (2014), Konradsen and Ouren (2014), Mullins et al. (2015), Komperød et al. (2015), and Hedlund (2015) are all based on the approach of identifying bitumen's viscoelastic properties in small-scale experiments, and then establishing the cables' and umbilicals' bending characteristics using first principle models. An alternative approach is to establish the bending characteristics directly from large-scale experiments on cables and umbilicals. The latter approach is considered in Maioli (2015), which presents interesting results on how the bending characteristic of a cable with bitumen-coated armor wires is influenced by bending curvature amplitude, bending curvature frequency, and the cable's temperature. Tarnowski (2015) also provides interesting considerations on identification of cables' dynamic bending characteristics through large-scale testing on cable segments.

Identification of materials' viscoelastic properties is widely covered in the literature. See (2001) provides an interesting survey on this topic. Olsen et al. (2014), as well as Konradsen and Ouren (2014), present identification of bitumen's viscoelastic properties based on rheometers. According to Konradsen and Ouren (2014), traditional low-strain rheometers typically operates in the shear strain range of 1% or less, while bitumen's shear strain in cables may be up to 500%. Hence, the viscoelastic properties established in low-strain rheometers may not be representative for bitumen's behavior in cables. Nexans Norway AS has therefore developed a laboratory instrument which is able to measure bitumen's viscoelastic properties at equally large shear strain as in real-life cables. This laboratory instrument is presented in Komperød et al. (2015).

In addition to the physical laboratory instrument, Komperød et al. (2015) also presents the mathematical derivation for how to calculate bitumen's viscoelastic properties from the logged measurements of the laboratory instrument. This derivation is based on a few assumptions and simplification that are valid for the temperature range of +5°C to +20°C, which is the temperature range considered in that publication. However, as bitumen's viscoelastic properties are highly temperature-dependent, one of this assumptions may become invalid for lower temperatures.

The contribution of the present paper is to improve the above mentioned mathematical derivation to also hold for bitumen at lower temperatures than +5°C. If the geometry or the materials of the laboratory instrument are changed, the improvement may also be necessary for temperatures of +5°C and above. The improvement is explained in more detail in Section 4, after the basic principle of the instrument has been presented in Section 3.

2 Nomenclature

Table 1 presents the symbols used in this paper. Complex numbers are indicated with tilde, for example $\tilde{G}$. The variables $\tilde{F}$, $\tilde{f}$, $\tilde{u}$, $\tilde{v}$, $\tilde{\gamma}$, $\tilde{\varepsilon}$, $\tilde{\sigma}$, and $\tilde{\tau}$ are phase vectors (phasors), i.e. complex number representations of variables changing with time in sinusoidal manners. The product EA is the rod's axial stiffness. The functions $\Re(\cdot)$ and $\Im(\cdot)$ return the real part and imaginary part, respectively, of their arguments.

3 Basic Principle of the Laboratory Instrument

This section explains briefly the basic principle of the laboratory instrument used to establish bitumen's viscoelastic properties at equally large shear strain as in subsea cables and umbilicals. For a more thorough explanation please refer to Komperød et al. (2015).

The laboratory instrument consists of a steel cylinder, a steel rod, a servomotor, and two sensors. The rod is inserted into the cylinder, and then axially and radially centered. Then the volume between the rod's outer surface and the cylinder's inner surface is filled with bitumen so that bitumen sticks to both surfaces. Figure 2 shows a side-view of the cylinder and the rod with bitumen.

Figure 2. Basic principle of the laboratory instrument.

The servomotor moves the rod axially, i.e. in left / right direction of Figure 2, in a sinusoidal manner. The sensors measure the displacement of the rod and the axial force required to achieve this displacement. These measurements are logged as timeseries in a computer.

The dashed lines of Figure 2 show the coordinate system to be used in this paper. The s coordinate is a Cartesian coordinate that represents the length parameter of the cylinder. At the left end of the cylinder $s = 0$, while on the right end of the cylinder $s = L$, where L is the length of the cylinder. The r coordinate is the radial coordinate of a polar coordinate system oriented normal to the s-axis. In the center of the rod $r = 0$. At the inner radius of the

DOI 10.3384/ecp1511943

Table 1. Nomenclature.

A	Rod's cross section area [m^2], $A = \pi {r_i}^2$.
$\tilde{c}_1$, $\tilde{c}_2$	Solution constants of ODE Eq. 29 [N].
E	Rod's elastic modulus [Pa].
$\tilde{F}(s)$	Axial tension in rod [N].
$\tilde{f}(s)$	General function of s [m].
$\tilde{G}$	Complex shear modulus of bitumen [Pa].
G^*	$G^* = \lvert\tilde{G}\rvert$ [Pa].
G'	$G' = \Re(\tilde{G})$ [Pa].
G''	$G'' = \Im(\tilde{G})$ [Pa].
$\tilde{H}$	Defined in Eq. 40 [N/m].
j	Imaginary unit [-], $j^2 \stackrel{\text{def}}{=} -1$.
L	Length of cylinder [m].
$\tilde{Q}$	Defined in Eq. 24 [m^{-1}].
$\tilde{Q}_1, \tilde{Q}_2$	Solutions of Eq. 24 w.r.t. $\tilde{Q}$ [m^{-1}].
Q'	$Q' = \Re(\tilde{Q}_1)$ [m^{-1}].
Q''	$Q'' = \Im(\tilde{Q}_1)$ [m^{-1}].
r	Radial coordinate [m].
r_i	Inner radius of bitumen layer [m].
r_o	Outer radius of bitumen layer [m].
s	Axial coordinate [m].
$\tilde{u}(r,s)$	Displacement of bitumen in direction parallel to rod's length [m].
$\tilde{v}(s)$	Axial displacement of rod [m].
$\tilde{\gamma}(r,s)$	Shear strain of bitumen [-].
$\tilde{\varepsilon}(s)$	Axial strain of rod [-].
$\tilde{\sigma}(s)$	Axial stress of rod [Pa].
$\tilde{\tau}(r,s)$	Shear stress of bitumen [Pa].
φ	$\varphi = \arg(\tilde{G})$ [rad].

bitumen layer, i.e. the outer radius of the rod, $r = r_i$. At the outer radius of the bitumen layer, i.e. the inner radius of the cylinder, $r = r_o$.

The servomotor and the two sensors are located at the right end, i.e. at $s = L$. Hence, the sensors measures the force $F(L)$ and the displacement $v(L)$, respectively. The contribution of this paper is to derive how to identify bitumen's viscoelastic properties from the logged time series of these two sensors.

4 Assumptions and Simplifications

As stated in Section 1, the mathematical derivation of Komperød et al. (2015) is based on a few assumptions and simplification, of which one may not hold for bitumen at lower temperatures. The assumption that may not hold is to disregard the axial strain of the rod in Figure 2. That is: At higher temperatures, bitumen has a low shear stress amplitude to shear strain amplitude ratio, G^*. Then a certain displacement of the rod requires only a small force by the servomotor. However, at lower temperatures bitumen has a very large G^*. A large axial force is then required to achieve the same displacement.

Due to the steel rod's inherent material properties, the rod will be strained when being axially tensioned. Because the force of the servomotor, and hence the tension of the rod, are low at high temperatures, the strain of the rod can be neglected. However, at low temperatures the tension and the axial strain of the rod are high, hence, the axial strain should therefore be included in the mathematical derivation.

In other words: The contribution of the present paper is to improve the mathematical derivation of Komperød et al. (2015) to also include the effect of axial strain of the steel rod. This improvement may also be necessary subject to changes of the laboratory instrument's geometry or materials.

The mathematical derivation of the present paper is subject to the following assumptions and simplifications:

1. Bitumen's shear stress and shear strain are assumed to be related through a complex shear modulus, i.e. $\tilde{\tau} = \tilde{G}\tilde{\gamma}$. The modulus may be a function of the shear strain amplitude, the shear strain frequency, and the temperature of bitumen. Further, the phase shift of the modulus, φ, is assumed to be in the half-open interval $\varphi \in \left[0\,,\,\frac{\pi}{2}\right)$.

2. The normal stress of bitumen in axial direction is neglected, because the force caused by this stress is neglectable compared to the axial force of the steel rod.

3. The force required to accelerate the rod and bitumen is disregarded, because this force is neglectable compared to the force required to strain bitumen.

4. The axial stress and axial strain of the steel rod are assumed to be related through a constant non-complex modulus, i.e. $\tilde{\sigma} = E\tilde{\varepsilon}$.

5. The cylinder is assumed to be fixed and rigid; any strain in the cylinder is neglected.

6. The Poisson ratio effect is neglected for the cylinder, the rod, and bitumen.

5 Identification of Viscoelastic Properties from Sensor Measurements

This section derives how to identify bitumen's viscoelastic properties from the timeseries logged by the two sensors of the laboratory instrument. The sensors measure the axial force, $F(L)$, and the axial displacement, $v(L)$, at the end of the rod shown to the right in Figure 2.

The parameter to be identified is the complex shear modulus of bitumen, $\tilde{G}$. From $\tilde{G}$ it is trivial to calculate the shear stress amplitude to shear strain amplitude ratio, G^*, the phase shift between shear stress and shear strain, φ, the storage modulus, G', and the loss modulus, G'', through the identity

$$\begin{aligned}\tilde{G} &= G^* e^{j\varphi} \\ &= G^*[\cos(\varphi) + j\sin(\varphi)] \\ &= G' + jG''.\end{aligned} \tag{1}$$

5.1 Equilibrium of a Rod Segment

Assume a rod segment of infinitesimal length ∂s. In one end of the segment the axial tension is $\tilde{F}(s)$ and in the other end the axial tension is $\tilde{F}(s) + \partial\tilde{F}(s)$. The circumferential surface of the rod sticks to bitumen giving a shear stress $\tilde{\tau}(r_i, s)$. This surface has an area of $2\pi r_i \partial s$. Hence, the shear force acting between bitumen and the rod over the segment length ∂s is $2\pi r_i \tilde{\tau}(r_i, s)\partial s$. This is illustrated in Figure 3.

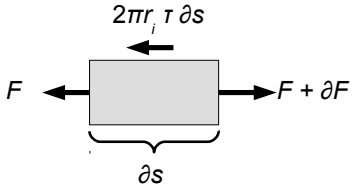

Figure 3. Forces acting of a rod segment of infinitesimal length ∂s.

By assumption 3 of Section 4, the force required to accelerate the rod and bitumen is neglectable. The following equilibrium is therefore stated

$$\tilde{F}(s) + \partial\tilde{F}(s) = \tilde{F}(s) + 2\pi r_i \tilde{\tau}(r_i, s)\partial s. \tag{2}$$

Cancelling and rewriting gives

$$\frac{\partial\tilde{F}(s)}{\partial s} = 2\pi r_i \tilde{\tau}(r_i, s). \tag{3}$$

The axial tension is related to the axial strain by $\tilde{F} = EA\tilde{\varepsilon}$. Further, the axial strain is related to the axial displacement by $\tilde{\varepsilon} = \frac{\partial\tilde{v}(s)}{\partial s}$. Hence, Eq. 3 can be rewritten to

$$EA\frac{\partial^2\tilde{v}(s)}{\partial s^2} = 2\pi r_i \tilde{\tau}(r_i, s). \tag{4}$$

Bitumen's shear stress is related to the shear strain through the complex modulus, i.e. $\tilde{\tau}(r,s) = \tilde{G}\tilde{\gamma}(r,s)$. The shear strain is related to the displacement by $\tilde{\gamma}(r,s) = -\frac{\partial\tilde{u}(r,s)}{\partial r}$. Inserting into Eq. 4 gives

$$EA\frac{\partial^2\tilde{v}(s)}{\partial s^2} = -2\pi r_i \tilde{G}\left.\frac{\partial\tilde{u}(r,s)}{\partial r}\right|_{r=r_i}. \tag{5}$$

5.2 Equilibrium of a Bitumen Segment

Consider a cylinder-shaped segment of bitumen with inner radius r, outer radius $r + \partial r$, and length ∂s. The shear force acting on the inner surface of the cylinder-shaped segment is $2\pi r\partial s\tilde{\tau}(r,s)$. The shear force acting on the outer surface is $2\pi[r + \partial r]\partial s[\tilde{\tau}(r,s) + \partial\tilde{\tau}(r,s)]$. By assumptions 2 and 3 of Section 4 the bitumen segment is in equilibrium by

$$2\pi r\partial s\tilde{\tau}(r,s) = 2\pi[r + \partial r]\partial s[\tilde{\tau}(r,s) + \partial\tilde{\tau}(r,s)]. \tag{6}$$

Canceling, simplifying, and disregarding the term $\partial r\,\partial\tilde{\tau}(r,s)$ gives

$$r\,\partial\tilde{\tau}(r,s) = -\partial r\,\tilde{\tau}(r,s), \tag{7}$$

$$r\tilde{G}\,\partial\tilde{\gamma}(r,s) = -\partial r\,\tilde{G}\,\tilde{\gamma}(r,s), \tag{8}$$

$$r\,\partial\tilde{\gamma}(r,s) = -\partial r\,\tilde{\gamma}(r,s), \tag{9}$$

$$-r\frac{\partial\tilde{\gamma}(r,s)}{\partial r} = \tilde{\gamma}(r,s), \tag{10}$$

$$-r\frac{\partial^2\tilde{u}(r,s)}{\partial r^2} = \frac{\partial\tilde{u}(r,s)}{\partial r}. \tag{11}$$

In Eq. 8 it is used that $\tilde{\tau}(r,s) = \tilde{G}\tilde{\gamma}(r,s)$, and in Eq. 11 it is used that $\tilde{\gamma}(r,s) = -\frac{\partial\tilde{u}(r,s)}{\partial r}$.

5.3 Establishing an ODE

In this section an ordinary differential equation (ODE) is established based on the results from Sections 5.1 and 5.2.

Integrating Eq. 11 w.r.t. r gives

$$-\int r\frac{\partial^2\tilde{u}(r,s)}{\partial r^2}\partial r = \int\frac{\partial\tilde{u}(r,s)}{\partial r}\partial r, \tag{12}$$

$$-\left[r\frac{\partial\tilde{u}(r,s)}{\partial r} - \int\frac{\partial\tilde{u}(r,s)}{\partial r}\partial r\right] = \int\frac{\partial\tilde{u}(r,s)}{\partial r}\partial r, \tag{13}$$

$$-r\frac{\partial\tilde{u}(r,s)}{\partial r} = \tilde{f}(s). \tag{14}$$

DOI 10.3384/ecp1511943

In Eq. 13 integration by parts is used for the left hand side of Eq. 12. The function $\tilde{f}(s)$ of Eq. 14 is the constant of integration, which is independent of r, but may be a function of s. Eq. 14 is an important result which states that the product $r\frac{\partial\tilde{u}(r,s)}{\partial r}$ is constant over the interval $r \in [\, r_i \,,\, r_o \,]$. Hence, Eq. 14 also holds for $r = r_i$. That is

$$-r_i \left.\frac{\partial\tilde{u}(r,s)}{\partial r}\right|_{r=r_i} = \tilde{f}(s). \tag{15}$$

Inserting Eq. 15 into Eq. 5 gives

$$EA\frac{\mathrm{d}^2\tilde{v}(s)}{\mathrm{d}s^2} = 2\pi\tilde{G}\,\tilde{f}(s). \tag{16}$$

In Eq. 16 the partial derivatives of Eq. 5 are replaced by ordinary derivatives as there is no longer any dependency on r in the differential equation.

The next issue is to identify the unknown function $\tilde{f}(s)$. Eq. 14 can be rewritten to

$$\partial\tilde{u}(r,s) = -\tilde{f}(s)\frac{\partial r}{r}. \tag{17}$$

Integrating w.r.t. r with integration limits r_i and r_o gives

$$\int_{r=r_i}^{r=r_o} \partial\tilde{u}(r,s) = -\tilde{f}(s)\int_{r_i}^{r_o}\frac{\partial r}{r}, \tag{18}$$

$$\begin{aligned}\tilde{u}(r_o,s) - \tilde{u}(r_i,s) &= -\tilde{f}(s)\,[\ln(r_o) - \ln(r_i)] \\ &= -\tilde{f}(s)\ln\left(\frac{r_o}{r_i}\right).\end{aligned} \tag{19}$$

Bitumen sticks to the inner surface of the cylinder, which is fixed. Hence, $\tilde{u}(r_o,s) = 0$. Further, bitumen also sticks to the rod. Therefore, $\tilde{u}(r_i,s) = \tilde{v}(s)$. Eq. 19 then simplifies to

$$\tilde{v}(s) = \tilde{f}(s)\ln\left(\frac{r_o}{r_i}\right). \tag{20}$$

Rewriting gives

$$\tilde{f}(s) = \frac{\tilde{v}(s)}{\ln\left(\frac{r_o}{r_i}\right)}. \tag{21}$$

Then inserting Eq. 21 into Eq. 16

$$EA\frac{\mathrm{d}^2\tilde{v}(s)}{\mathrm{d}s^2} = \frac{2\pi\tilde{G}}{\ln\left(\frac{r_o}{r_i}\right)}\,\tilde{v}(s), \tag{22}$$

$$\frac{\mathrm{d}^2\tilde{v}(s)}{\mathrm{d}s^2} - \frac{2\pi\tilde{G}}{EA\ln\left(\frac{r_o}{r_i}\right)}\,\tilde{v}(s) = 0. \tag{23}$$

Eq. 23 is a second order, linear, homogeneous differential equation with constant coefficient written on standard form. However, note that the coefficient is complex.

To simplify the notation, the variable $\tilde{Q}$ is introduced, which is defined implicitly as

$$\tilde{Q}^2 \overset{\text{def}}{=} \frac{2\pi\tilde{G}}{EA\ln\left(\frac{r_o}{r_i}\right)}. \tag{24}$$

Using $\tilde{Q}$, Eq. 23 becomes

$$\frac{\mathrm{d}^2\tilde{v}(s)}{\mathrm{d}s^2} - \tilde{Q}^2\,\tilde{v}(s) = 0. \tag{25}$$

Differentiating Eq. 25 w.r.t. s gives

$$\frac{\mathrm{d}^3\tilde{v}(s)}{\mathrm{d}s^3} - \tilde{Q}^2\,\frac{\mathrm{d}\tilde{v}(s)}{\mathrm{d}s} = 0, \tag{26}$$

$$\frac{\mathrm{d}^2\tilde{\varepsilon}(s)}{\mathrm{d}s^2} - \tilde{Q}^2\,\tilde{\varepsilon}(s) = 0, \tag{27}$$

$$EA\frac{\mathrm{d}^2\tilde{\varepsilon}(s)}{\mathrm{d}s^2} - EA\,\tilde{Q}^2\,\tilde{\varepsilon}(s) = 0, \tag{28}$$

$$\frac{\mathrm{d}^2\tilde{F}(s)}{\mathrm{d}s^2} - \tilde{Q}^2\,\tilde{F}(s) = 0. \tag{29}$$

In Eq. 27 it is used that $\tilde{\varepsilon} = \frac{\mathrm{d}\tilde{v}(s)}{\mathrm{d}s}$, and in Eq. 29 it is used that $\tilde{F} = EA\,\tilde{\varepsilon}$. It is trivial to verify that the solution of Eq. 29 is

$$\tilde{F}(s) = \tilde{c}_1 e^{\tilde{Q}s} + \tilde{c}_2 e^{-\tilde{Q}s}. \tag{30}$$

5.4 Boundary Conditions

The most common way to apply boundary conditions to an ODE on the form of Eq. 30 is to solve for $\tilde{c}_1$ and $\tilde{c}_2$ using two boundary conditions. However, the problem formulation of the present paper is somewhat different: The final goal is to identify $\tilde{G}$ from timeseries logged by the sensors presented in Section 3. As $\tilde{G}$ can easily be found from known $\tilde{Q}$ using Eq. 24, goal is to identify $\tilde{Q}$.

The problem to be solved has three unknowns: $\tilde{c}_1$, $\tilde{c}_2$, and $\tilde{Q}$. There are also three boundary conditions available:

1. There is no force acting on the left side of the rod in Figure 2. Hence, $\tilde{F}(0) = 0$.
2. The force acting on the right side of the rod, $\tilde{F}(L)$, is known because it is logged from the force sensor.

3. The displacement of the right side of the rod, $\tilde{v}(L)$, is known because it is logged from the displacement sensor.

Inserting boundary condition 1 into Eq. 30

$$\tilde{F}(0) = \tilde{c}_1 e^{\tilde{Q}\cdot 0} + \tilde{c}_2 e^{-\tilde{Q}\cdot 0}, \tag{31}$$

$$0 = \tilde{c}_1 \cdot 1 + \tilde{c}_2 \cdot 1, \tag{32}$$

$$\tilde{c}_2 = -\tilde{c}_1. \tag{33}$$

Then inserting Eq. 33 into Eq. 30

$$\begin{aligned}\tilde{F}(s) &= \tilde{c}_1 \left[e^{\tilde{Q}s} - e^{-\tilde{Q}s}\right] \\ &= 2\tilde{c}_1 \sinh(\tilde{Q}s).\end{aligned} \tag{34}$$

Differentiating Eq. 34 w.r.t. s gives

$$\frac{\mathrm{d}\tilde{F}(s)}{\mathrm{d}s} = 2\tilde{c}_1\tilde{Q}\cosh(\tilde{Q}s), \tag{35}$$

$$EA\frac{\mathrm{d}\tilde{\varepsilon}(s)}{\mathrm{d}s} = 2\tilde{c}_1\tilde{Q}\cosh(\tilde{Q}s), \tag{36}$$

$$\frac{\mathrm{d}^2\tilde{v}(s)}{\mathrm{d}s^2} = \frac{2\tilde{c}_1}{EA}\tilde{Q}\cosh(\tilde{Q}s), \tag{37}$$

where $\tilde{F} = EA\,\tilde{\varepsilon}$ is used in Eq. 36, and $\tilde{\varepsilon} = \frac{\mathrm{d}\tilde{v}(s)}{\mathrm{d}s}$ is used in Eq. 37. Inserting Eq. 25 into Eq. 37

$$\tilde{Q}^2\tilde{v}(s) = \frac{2\tilde{c}_1}{EA}\tilde{Q}\cosh(\tilde{Q}s), \tag{38}$$

$$\tilde{v}(s) = \frac{2\tilde{c}_1}{EA}\frac{\cosh(\tilde{Q}s)}{\tilde{Q}}. \tag{39}$$

As explained in Section 3, the rod is moved in a sinusoidal manner by the servomotor. Hence, $\tilde{v}(L)$ is a sinusoidal signal. Further, according to Komperød et al. (2015), the signal of the measured force, $\tilde{F}(L)$, can be well approximated by a sinus curve of the same frequency as $\tilde{v}(L)$, but with different amplitude and different phase. It is then convenient to define the $\tilde{H}$ as the complex ratio

$$\tilde{H} \overset{\text{def}}{=} \frac{\tilde{F}(L)}{\tilde{v}(L)}. \tag{40}$$

Hence, $\tilde{H}$ is a complex number expressing the force amplitude to displacement amplitude ratio, and the phase shift between the force and the displacement. Komperød et al. (2015) explain how to find $\tilde{H}$ from the logged measurement data.

Setting $s = L$ in Eqs. 34 and 39, and inserting these equations into Eq. 40 gives

$$\tilde{H} = \frac{2\tilde{c}_1 \sinh(\tilde{Q}L)}{\frac{2\tilde{c}_1}{EA}\frac{\cosh(\tilde{Q}L)}{\tilde{Q}}}, \tag{41}$$

$$\tilde{H} = EA\,\tilde{Q}\tanh(\tilde{Q}L). \tag{42}$$

Eq. 42 is the main result of this paper. This nonlinear equation in one complex variable relates $\tilde{Q}$ to the measured force and measured displacement at the rod's right end in Figure 2. The non-complex parameters E, A, and L are known, while $\tilde{H}$ can be established from the sensor measurements. When $\tilde{Q}$ is identified, the viscoelastic properties of bitumen can easily be established through Eq. 24, and thereafter using Eq. 1.

As Eq. 42 is a complex equation, real part on both sides must be equal, and the imaginary part on both sides must be equal. Hence, Eq. 42 can be decomposed into two nonlinear equations

$$\Re\left(\tilde{H}\right) = \Re\left(EA\,\tilde{Q}\tanh(\tilde{Q}L)\right), \tag{43}$$

$$\Im\left(\tilde{H}\right) = \Im\left(EA\,\tilde{Q}\tanh(\tilde{Q}L)\right). \tag{44}$$

How to solve the nonlinear, complex Eq. 42 w.r.t. $\tilde{Q}$, or equivalently to solve Eqs. 43 and 44, using for example a numerical method, is beyond the scope of this paper.

The next two sections provide analytical approximations that are valid for small values of $|\tilde{Q}L|$, and for large values of $|\tilde{Q}L|$, respectively. Using these approximations, it is trivial to solve Eq. 42 analytically. The solutions based on the approximations give very useful information about the relationship between $\tilde{Q}$ and $\tilde{H}$, which is of both theoretical and practical interest. Further, these solution may be good initial values for numerical solution of Eq. 42. Please note that there may be an interval between "small values" and "large values", where both approximations give inaccurate estimates of $\tilde{Q}$.

5.5 Approximation for Small Values of $|\tilde{Q}L|$

If $|\tilde{Q}L|$ is small, then $\tanh(\tilde{Q}L)$ can be approximated by a Maclaurin series expansion. The Maclaurin series of $\tanh(\tilde{z})$ is known to converge for $|\tilde{z}| < \frac{\pi}{2}$, where $\tilde{z}$ is a complex number. The first order Maclaurin polynomial is

$$\tanh(\tilde{Q}L) \approx \tilde{Q}L. \tag{45}$$

Inserting Eq. 45 into Eq. 42

$$\begin{aligned}\tilde{H} &= EA\,\tilde{Q}\cdot\tilde{Q}L \\ &= EAL\,\tilde{Q}^2.\end{aligned} \tag{46}$$

That is

$$\tilde{Q}^2 = \frac{\tilde{H}}{EAL}. \tag{47}$$

DOI 10.3384/ecp1511943

5.6 Approximation for Large Values of $|\tilde{Q}L|$

The function $\tanh(\tilde{z})$ is by definition

$$\begin{aligned}\tanh(\tilde{z}) &\stackrel{\text{def}}{=} \frac{\sinh(\tilde{z})}{\cosh(\tilde{z})} \\ &= \frac{\frac{e^{\tilde{z}}-e^{-\tilde{z}}}{2}}{\frac{e^{\tilde{z}}+e^{-\tilde{z}}}{2}} \\ &= \frac{e^{\tilde{z}}-e^{-\tilde{z}}}{e^{\tilde{z}}+e^{-\tilde{z}}}.\end{aligned} \tag{48}$$

The right hand side of Eq. 24 are real, except for the factor $\tilde{G}$. Hence,

$$\arg(\tilde{Q}^2) = \arg(\tilde{G}) \in \left[0\,,\,\frac{\pi}{2}\right), \tag{49}$$

$$\arg(\tilde{Q}_1) = \frac{1}{2}\arg(\tilde{G}) \in \left[0\,,\,\frac{\pi}{4}\right), \tag{50}$$

$$\arg(\tilde{Q}_2) = \frac{1}{2}\arg(\tilde{G}) + \pi \in \left[\pi\,,\,\frac{5\pi}{4}\right), \tag{51}$$

where $\tilde{Q}_1$ and $\tilde{Q}_2$ are the two solutions of Eq. 24. The interval of Eq. 49 follows from Assumption 1 of Section 4, while the other two intervals follow from the first one using the nth root of unity. Comparing Eq. 50 and Eq. 51 shows that

$$\tilde{Q}_2 = -\tilde{Q}_1, \tag{52}$$

because $\tilde{Q}_1$ and $\tilde{Q}_2$ have the same magnitude. Now using the notation

$$\tilde{Q}_1 = Q' + jQ'', \tag{53}$$

$$\tilde{Q}_2 = -Q' - jQ'', \tag{54}$$

where $Q', Q'' \in \mathbb{R}$, and $Q' > Q'' \geq 0$. Considering the limit of $\tanh(\tilde{Q}_1 L)$ as $|\tilde{Q}_1| \to \infty$

$$\begin{aligned}&\lim_{|\tilde{Q}_1|\to\infty} \tanh(\tilde{Q}_1 L) \\ &= \lim_{|\tilde{Q}_1|\cos(\arg(\tilde{Q}_1))\to\infty} \tanh(\tilde{Q}_1 L) \\ &= \lim_{Q'\to\infty} \tanh(\tilde{Q}_1 L) \\ &= \lim_{Q'\to\infty} \frac{e^{\tilde{Q}_1 L} - e^{-\tilde{Q}_1 L}}{e^{\tilde{Q}_1 L} + e^{-\tilde{Q}_1 L}} \\ &= \lim_{Q'\to\infty} \frac{e^{Q'L+jQ''L} - e^{-Q'L-jQ''L}}{e^{Q'L+jQ''L} + e^{-Q'L-jQ''L}} \\ &= \lim_{Q'\to\infty} \frac{e^{Q'L}e^{jQ''L} - e^{-Q'L}e^{-jQ''L}}{e^{Q'L}e^{jQ''L} + e^{-Q'L}e^{-jQ''L}} \\ &= \frac{\lim_{Q'\to\infty} e^{Q'L}e^{jQ''L} - \lim_{Q'\to\infty} e^{-Q'L}e^{-jQ''L}}{\lim_{Q'\to\infty} e^{Q'L}e^{jQ''L} + \lim_{Q'\to\infty} e^{-Q'L}e^{-jQ''L}} \\ &= \frac{\lim_{Q'\to\infty} e^{Q'L}e^{jQ''L} - 0}{\lim_{Q'\to\infty} e^{Q'L}e^{jQ''L} + 0} \\ &= 1.\end{aligned} \tag{55}$$

Next, considering the limit of $\tanh(\tilde{Q}_2 L)$ as $|\tilde{Q}_2| \to \infty$

$$\begin{aligned}&\lim_{|\tilde{Q}_2|\to\infty} \tanh(\tilde{Q}_2 L) \\ &= \lim_{-|\tilde{Q}_2|\cos(\arg(\tilde{Q}_2))\to\infty} \tanh(\tilde{Q}_2 L) \\ &= \lim_{-(-Q')\to\infty} \tanh(\tilde{Q}_2 L) \\ &= \lim_{Q'\to\infty} \tanh(\tilde{Q}_2 L) \\ &= \lim_{Q'\to\infty} \frac{e^{\tilde{Q}_2 L} - e^{-\tilde{Q}_2 L}}{e^{\tilde{Q}_2 L} + e^{-\tilde{Q}_2 L}} \\ &= \lim_{Q'\to\infty} \frac{e^{-Q'L-jQ''L} - e^{Q'L+jQ''L}}{e^{-Q'L-jQ''L} + e^{Q'L+jQ''L}} \\ &= \lim_{Q'\to\infty} \frac{e^{-Q'L}e^{-jQ''L} - e^{Q'L}e^{jQ''L}}{e^{-Q'L}e^{-jQ''L} + e^{Q'L}e^{jQ''L}} \\ &= \frac{\lim_{Q'\to\infty} e^{-Q'L}e^{-jQ''L} - \lim_{Q'\to\infty} e^{Q'L}e^{jQ''L}}{\lim_{Q'\to\infty} e^{-Q'L}e^{-jQ''L} + \lim_{Q'\to\infty} e^{Q'L}e^{jQ''L}} \\ &= \frac{0 - \lim_{Q'\to\infty} e^{Q'L}e^{jQ''L}}{0 + \lim_{Q'\to\infty} e^{Q'L}e^{jQ''L}} \\ &= -1.\end{aligned} \tag{56}$$

That is, when using the solution $\tilde{Q}_1$ of Eq. 24, then for large magnitude of $\tilde{Q}_1 L$, Eq. 42 can be approximated by

$$\begin{aligned}\tilde{H} &= EA\,\tilde{Q}_1 \cdot \lim_{|\tilde{Q}_1|\to\infty} \tanh(\tilde{Q}_1 L) \\ &= EA\,\tilde{Q}_1 \cdot 1 \\ &= EA\,\tilde{Q}_1.\end{aligned} \tag{57}$$

When using the solution $\tilde{Q}_2$ of Eq. 24, then the approximation for large $\tilde{Q}_2 L$ becomes

$$\begin{aligned}\tilde{H} &= EA\,\tilde{Q}_2 \cdot \lim_{|\tilde{Q}_2|\to\infty} \tanh(\tilde{Q}_2 L) \\ &= EA\,\tilde{Q}_2 \cdot (-1) \\ &= -EA\,\tilde{Q}_2.\end{aligned} \tag{58}$$

Inserting Eq. 52 into Eq. 58 gives

$$\tilde{H} = EA\,\tilde{Q}_1, \tag{59}$$

which is the same result as in Eq. 57. In other words: Both solutions of Eq. 24 yield the same approximation, i.e. Eq. 59. It is then trivial to solve for $\tilde{Q}$

$$\tilde{Q}_1 = \frac{\tilde{H}}{EA}, \tag{60}$$

$$\tilde{Q}_1{}^2 = \tilde{Q}_2{}^2 = \tilde{Q}^2 = \frac{\tilde{H}^2}{(EA)^2}, \tag{61}$$

which can be inserted into Eq. 24 to obtain $\tilde{G}$.

5.7 Summary

The problem that has been addressed is to identify $\tilde{Q}$ from logged sensor measurements of the rod's axial displacement and axial force at the right end of the rod, see Figure 2. The complex number $\tilde{H}$ expresses the force amplitude to displacement amplitude ratio, and the phase shift between the force and the displacement. The parameters E, A, L, r_i, and r_o are known.

When $\tilde{H}$ has been established from timeseries of the sensor measurements, $\tilde{Q}$ can be found from the complex, nonlinear Eq. 42, or from the nonlinear set of equations Eqs. 43 and 44. Small values of $|\tilde{Q}L|$ allow $\tilde{Q}$ to be approximated by Eq. 47. Large values of $|\tilde{Q}L|$ allow $\tilde{Q}$ to be approximated by Eq. 60. However, note that there may be an interval between "small values" and "large values" where both approximations are inaccurate. The approximations of Eq. 47 and Eq. 60 may be used as initial values when solving Eq. 42 numerically.

When $\tilde{Q}$ has been identified, the viscoelastic properties of bitumen can be found through Eq. 24, followed by Eq. 1.

6 Conformal Mapping

Although the function of Eq. 42 takes only one input parameter, $\tilde{Q}$, and gives one output, $\tilde{H}$, it is not possible to visualize the function in one (x,y) plot, because the input and the output have both a real part and an imaginary part each. Conformal mapping is an approach to visualize functions with complex inputs and outputs. Introductions to conformal mapping are given in books and other literatures on complex analysis, see for example Chapter 17 of Kreyszig (2011).

Conformal mapping of a function with one complex input and one complex output consists of two (x,y) plots: The input plot shows the real part of the input on the first axis (x-axis) and imaginary part of the input on the second axis (y-axis). The output plot shows the real part of the output on the first axis and imaginary part of the output on the second axis. In both plots it is drawn curves, often distinguished with different colors, line styles, or similar, such that a curve in the input plot represents a set of input values, and a corresponding curve in the output plot represents the corresponding set of output values. The plots may also include individual points, where one point in the output plot is the function evaluation of the corresponding point in the input plot.

6.1 Conformal Mapping of the Main Equation

The main result of this paper is Eq. 42, which can be rewritten to

$$\frac{\tilde{H}}{EA} = \tilde{Q}\tanh(\tilde{Q}L). \tag{62}$$

Figure 4 shows conformal mapping of Eq. 62. Each curve in the input plot represents a set of the input $\tilde{Q}$. The corresponding curve in the output plot, as distinguished by line color and line style, represents the corresponding set of the output $\frac{\tilde{H}}{EA}$. Also, each point marked by a circle or a square in the output plot is the function evaluation of the corresponding input in the input plot. In the input plot, each of the straight, solid lines with square markers corresponds to increasing magnitude of $\tilde{Q}$, while the argument is fixed. Each of the dashed lines with circle markers corresponds to fixed magnitude and variable argument.

Figure 4 shows that that for small $|\tilde{Q}|$ the output $\frac{\tilde{H}}{EA}$ has much larger argument than the input $\tilde{Q}$, i.e. the function $\frac{\tilde{H}}{EA} = \tilde{Q}\tanh(\tilde{Q}L)$ increases the argument, because the slopes of the solid curves are much steeper in the output plot than in the input plot for small $|\tilde{Q}|$. This can also be seen from the blue dashed curve with circle markers; this curve spans a larger angle in the output plot than in the input plot.

Further, Figure 4 shows that the the function $\frac{\tilde{H}}{EA} = \tilde{Q}\tanh(\tilde{Q}L)$ decreases the magnitude for small $|\tilde{Q}|$. This is seen from the fact that markers which are close to the

DOI 10.3384/ecp1511943

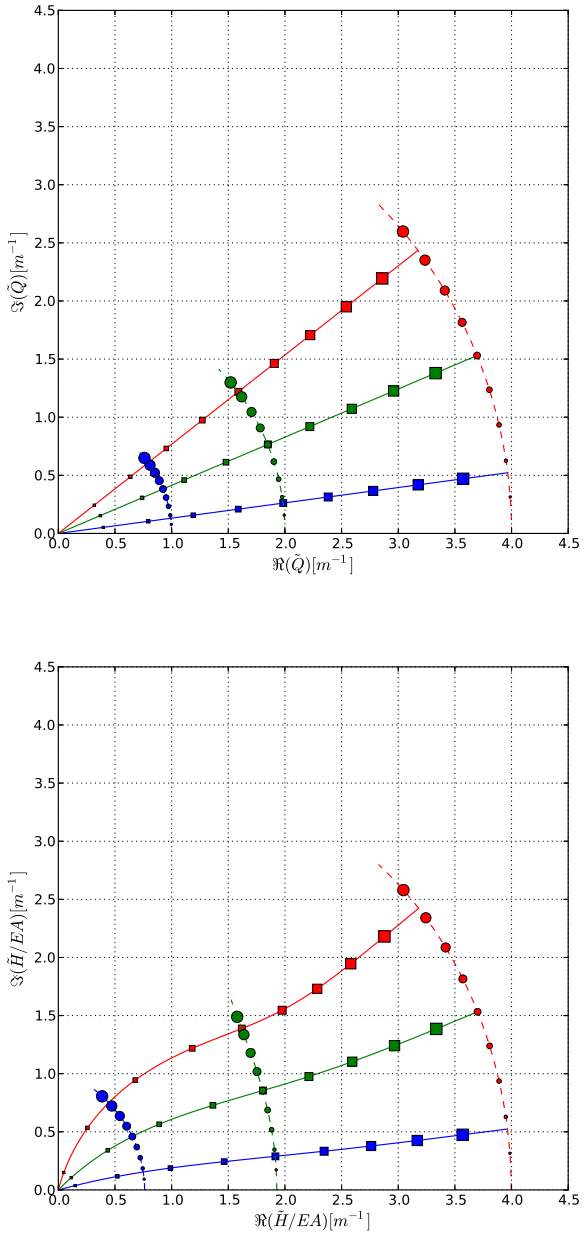

Figure 4. Conformal mapping of Eq. 62. The cylinder length is set to $L = 1.0$. The input plot (upper) shows the real part and the imaginary part of the input $\tilde{Q}$. The output plot (lower) shows the corresponding real part and imaginary part of the output $\frac{\tilde{H}}{EA}$. Please refer to the main text for further explanation.

origin in the input plot are even closer to the origin in the output plot.

The behavior of the function $\frac{\tilde{H}}{EA} = \tilde{Q}\tanh(\tilde{Q}L)$ as described in the previous two paragraphs is in accordance to the approximation for small values of $|\tilde{Q}L|$ presented in Section 5.5. Rewriting Eq. 47 gives

$$\frac{\tilde{H}}{EA} = \tilde{Q}^2 L, \tag{63}$$

which shows that the output corresponds to the input $\tilde{Q}$ squared. From theory on complex numbers it is known that squaring a complex number is identical to squaring the magnitude and doubling the argument.

For larger values of $|\tilde{Q}|$, it is seen from Figure 4 that the output of the function $\frac{\tilde{H}}{EA} = \tilde{Q}\tanh(\tilde{Q}L)$ is near identical to the input. This is seen by observing that the larger square markers of any colors, as well as the red circular markers of any sizes, have nearly identical coordinates in the output plot as in the input plot. This behavior is also seen by the approximation of $\frac{\tilde{H}}{EA} = \tilde{Q}\tanh(\tilde{Q}L)$ for large $|\tilde{Q}L|$, which is derived in Section 5.6. The approximation is

$$\frac{\tilde{H}}{EA} = \tilde{Q}_1, \tag{64}$$

which states that the output is identical to the input for large $|\tilde{Q}L|$, provided that $\arg(\tilde{Q})$ obeys Eq. 50. (If $\arg(\tilde{Q})$ instead obeys Eq. 51, the output will be the negative of the input as follows from Eq. 58.)

6.2 Conformal Mapping of Approximations

The conformal mapping presented in Section 6.1 are in accordance to the approximations for small $|\tilde{Q}L|$ and for large $|\tilde{Q}L|$ as derived in Sections 5.5 and 5.6, respectively. The present section compares the two approximations, Eq. 63 and Eq. 64, with the main function, Eq. 62.

Figure 5 compares the main function and the approximations for small values of $|\tilde{Q}|$. Please read the figure caption for explanation of the figure. It is seen that Eq. 63 (dashed curves) follows Eq. 62 (solid curves) very closely for small values of $|\tilde{Q}|$ as the markers of same size and same color lie on top of each other. However, as $|\tilde{Q}|$ increases, the markers and the curves begin to deviate. Figure 5 shows that the approximation which is valid for large values of $|\tilde{Q}L|$, i.e. Eq. 64, performs very poorly for small values of $|\tilde{Q}|$.

Please note that it is not sufficiently to compare the slopes of the curves: Comparing the coordinates for markers of the same size and the same color shows that the markers of Eq. 64 are located farther from the origin than the corresponding markers of the other two equations. Hence, Eq. 64 significantly overestimates the magnitude of the output, $\frac{\tilde{H}}{EA}$.

Figure 6 shows the approximations Eq. 63 and Eq. 64 for large values of $|\tilde{Q}|$. The approximation for large values, i.e. Eq. 64 (dotted curves), approaches Eq. 62 (solid curves) as $|\tilde{Q}|$ increases. For the largest $|\tilde{Q}|$ shown in the figure, the markers of Eq. 62 and Eq. 64 lie on top of each other. In Figure 6, the approximation for small values of $|\tilde{Q}L|$, i.e. Eq. 63 (dashed curves), gives a poor approximation, except for the lowest values of $|\tilde{Q}|$.

From Figure 5 and Figure 6 it is concluded that Eq. 63 is a good approximation of Eq. 62 for small values of $|\tilde{Q}L|$,

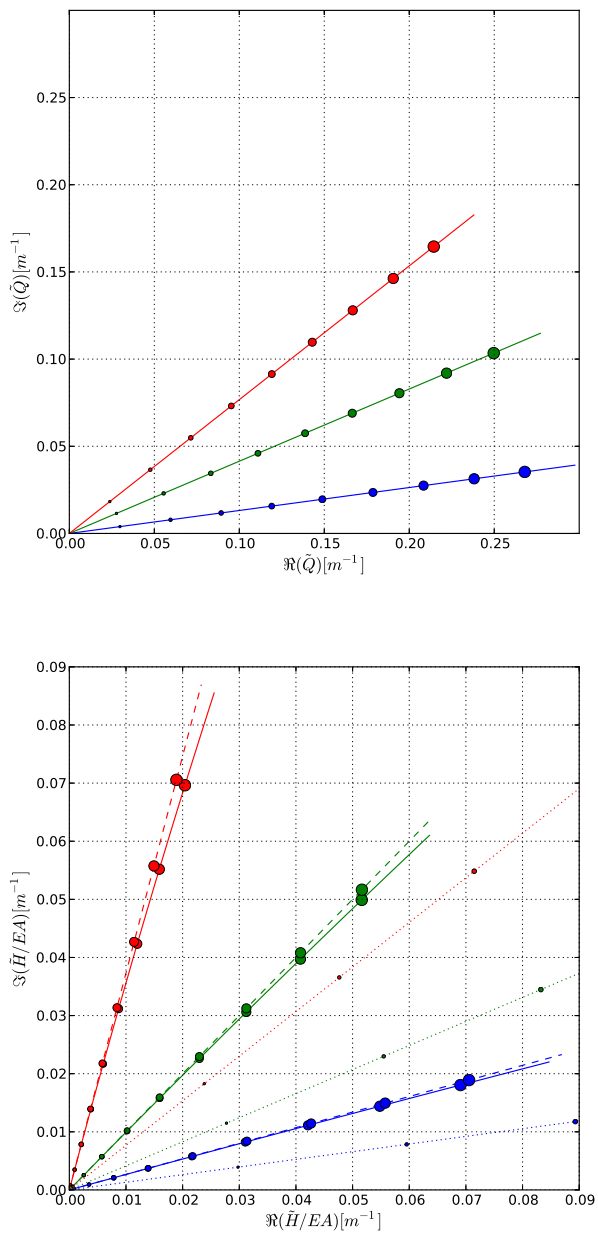

Figure 5. Conformal mapping for small values of $|\tilde{Q}|$ for the main function and the two approximations. The output plot (lower) shows the output of Eq. 62 (solid curves), Eq. 63 (dashed curves), and Eq. 64 (dotted curves). The input marked by red color in the input plot (upper) is used for all outputs marked by red color in the output plot, and similar for green color and blue color. The cylinder length is set to $L = 1.0$.

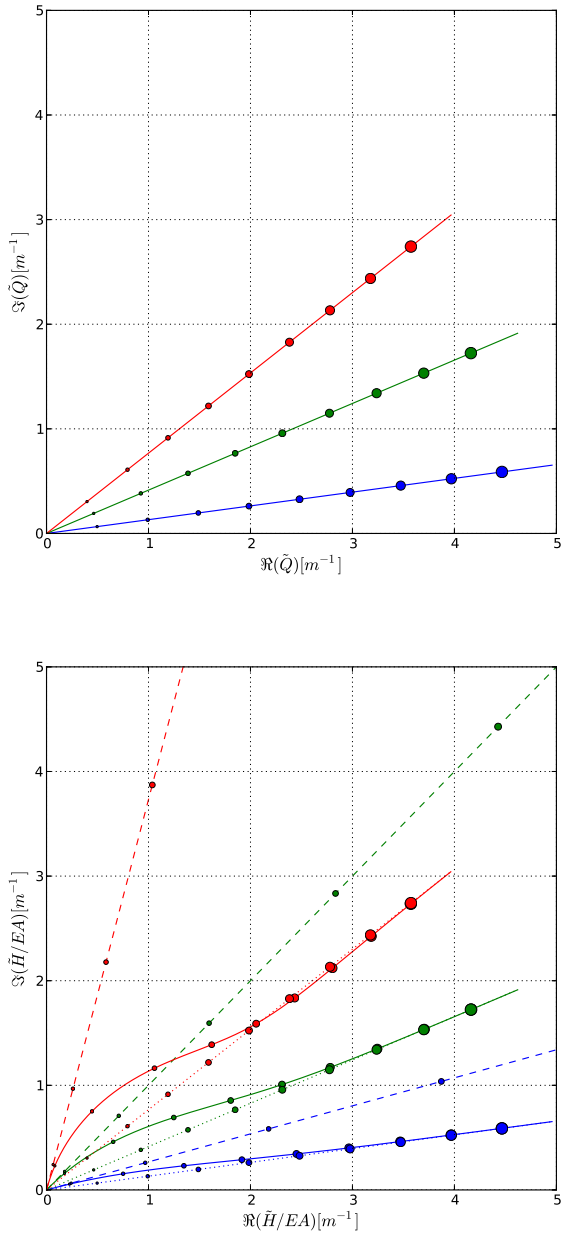

Figure 6. Conformal mapping for large values of $|\tilde{Q}|$ for the main function and the two approximations. The output plot (lower) shows the output of Eq. 62 (solid curves), Eq. 63 (dashed curves), and Eq. 64 (dotted curves). The input marked by red color in the input plot (upper) is used for all outputs marked by red color in the output plot, and similar for green color and blue color. The cylinder length is set to $L = 1.0$.

while Eq. 64 is a good approximation for large values of $|\tilde{Q}L|$. However, as can be seen from Figure 6, there is a range between "small values" and "large values" where both approximations are inaccurate.

7 Practical Interpretations

This section discusses the practical interpretations of the results derived in the present paper.

DOI 10.3384/ecp1511943

7.1 Comparison to Komperød et al. (2015)

Komperød et al. (2015) also derive how to identify the viscoelastic properties of bitumen based on timeseries of measured axial force and axial displacement of the rod in Figure 2. The main difference between the derivation of that paper and the present paper is that the former paper neglects axial strain in the rod, while the latter paper takes this effect into account. It is then of interest to compare the results of the two papers.

The derivation of Komperød et al. (2015) results in the following formula for identification of bitumen's viscoelastic properties

$$\tilde{G} = \frac{\ln\left(\frac{r_o}{r_i}\right)}{2\pi L}\tilde{H}. \tag{65}$$

The main result of the present paper is Eq. 42, which for small values of $|\tilde{Q}L|$ can be approximated by Eq. 46. Inserting Eq. 24 into Eq. 46 gives

$$\begin{aligned}\tilde{H} &= EAL\frac{2\pi\tilde{G}}{EA\ln\left(\frac{r_o}{r_i}\right)} \\ &= \frac{2\pi\tilde{G}L}{\ln\left(\frac{r_o}{r_i}\right)}.\end{aligned} \tag{66}$$

Solving Eq. 66 for $\tilde{G}$ gives Eq. 65. Hence, the result derived in Komperød et al. (2015) yields the exact same identification of bitumen's viscoelastic properties as the approximation for small $|\tilde{Q}L|$ which is derived in Section 5.5. In other words: The result of Komperød et al. (2015) may be used for identification of bitumen's viscoelastic properties if and only if Eq. 46 is a good approximation of Eq. 42. It is then of interest to understand when this approximation is good. Eq. 46 can be rewritten to

$$\frac{\tilde{H}L}{EA} = (\tilde{Q}L)^2, \tag{67}$$

which gives

$$\tilde{Q}L = \pm\sqrt{\frac{\tilde{H}L}{EA}}. \tag{68}$$

Note that the right hand side of Eq. 68 can be calculated from logged timeseries of sensor measurements and known parameters. The approximation of Section 5.5 is based on a first order Maclaurin approximation of $\tanh(\tilde{Q}L)$, i.e.

$$\tanh(\tilde{Q}L) \approx \tilde{Q}L. \tag{69}$$

Hence, the accuracy of the result from Komperød et al. (2015) can be evaluated by calculating $\tilde{Q}L$ from Eq. 68, and then comparing the right hand side of Eq. 69 with the left hand side. If the difference is small, then the formula of Komperød et al. (2015) can be used to identify bitumen's viscoelastic properties, otherwise Eq. 42 of the present paper should be used. The analyst must then make a judgment of what is sufficiently small difference to use the result of Komperød et al. (2015).

From Eq. 65 it is seen that when the approximation of Eq. 69 is used, $\tilde{G}$ and $\tilde{H}$ are related through a real constant. Hence, bitumen's shear stress amplitude to shear strain amplitude ratio, G^*, is proportional to the rod's axial force amplitude to axial displacement amplitude ratio, $|\tilde{H}|$. Further, the phase shift between bitumen's shear stress and shear strain, φ, is equal to the phase shift between the rod's axial force and axial displacement, $\arg(\tilde{H})$.

Please note that the length of the cylinder, L, strongly influences whether the results from Komperød et al. (2015) can be used or not. For a given value of $\tilde{Q}$, the approximation of Eq. 69 is more accurate for a smaller value of L. In other words: Using a shorter cylinder is beneficial in the sense that the results of Komperød et al. (2015) can be used for lower bitumen temperatures. Increasing the rod's axial stiffness, EA, has the same desired effect: It is seen from Eq. 24 that increasing EA decreases $|\tilde{Q}|$. Increasing the ratio $\frac{r_o}{r_i}$ also has this benefit.

The rod's axial stiffness, EA, is not included in Eq. 65. However, EA is required in Eq. 68 for evaluating whether Eq. 65 can be used or not.

7.2 Behavior of Approximation for Large $|\tilde{Q}L|$

As derived in Section 5.6, the approximation of Eq. 60 and Eq. 61 is valid for large $|\tilde{Q}L|$. Inserting Eq. 24 into Eq. 61 gives

$$\frac{2\pi\tilde{G}}{EA\ln\left(\frac{r_o}{r_i}\right)} = \frac{\tilde{H}^2}{(EA)^2}, \tag{70}$$

$$\tilde{G} = \frac{\ln\left(\frac{r_o}{r_i}\right)}{2\pi EA}\tilde{H}^2. \tag{71}$$

That is, $\tilde{G}$ is proportional to $\tilde{H}^2$. This means that the identified bitumen shear stress amplitude to shear strain amplitude ratio, G^*, is proportional to the square of the rod's axial force amplitude to axial displacement amplitude ratio, $|\tilde{H}|$. Further, the identified phase shift between bitumen's shear stress and shear strain, φ, is twice the phase shift between the force and the displacement, $\arg(\tilde{H})$. This behavior is different from the behavior at low $|\tilde{Q}L|$ as explained in Section 7.1. However, this difference was expected from comparison of the dashed and dotted curves of Figures 5 and 6.

8 Further Work

The present paper derives an improvement in identification in bitumen's viscoelastic properties. When these properties are identified for a sufficient range of shear strain amplitude, shear strain frequency, and bitumen temperature, the properties will be included in first principle models of the mechanical properties of subsea cables and umbilicals.

9 Conclusion

This paper derives an improved mathematical model for how to identify bitumen's viscoelastic properties from the laboratory instrument illustrated in Figure 2. The improvement compared to the model of Komperød et al. (2015) is that the axial strain of the rod is included in the derivation. This improvement is important when identifying bitumen's viscoelastic properties at low temperatures.

The main result of the present paper is a nonlinear equation in one complex variable that relates bitumen's viscoelastic properties to the sensor measurements of the laboratory instrument. Under certain conditions, approximations of this equation can be used, which makes it trivial to obtain explicit expressions for bitumen's viscoelastic properties. The nonlinear equation, as well as the approximations, are illustrated using conformal mapping. The solutions based on the approximations can be used as initial values if solving the nonlinear equation numerically.

It is proved mathematically that one of the approximations is identical to the model of Komperød et al. (2015). It is also established a mathematical criterion for when this result can be used.

The final purpose of identifying bitumen's viscoelastic properties is to include these properties in models of subsea cables' and umbilicals' mechanical properties.

References

M. Caire. Flexible riser bending hysteresis influence on bend stiffener response. In *Proceedings of the ASME 33rd International Conference on Ocean, Offshore and Arctic Engineering OMAE 2014*, 2014.

J. J. Féret and C. L. Bournazel. Calculation of stresses and slip in structural layers of unbonded flexible pipes. *Journal of Offshore Mechanics and Arctic Engineering*, 109:263 – 269, 1987.

J. Hedlund. Modelling of viscoelastic dynamic bending stiffness for VIV analysis of submarine cables. In *Proceedings of the 9th International Conference on Insulated Power Cables (Jicable '15)*, 2015.

M. Komperød, B. Konradsen, and R. Slora. Viscoelastic large strain model of bitumen used for corrosion protection in subsea cables and umbilicals. In *Proceedings of the ASME 2015 34th International Conference on Ocean, Offshore and Arctic Engineering OMAE 2015*, 2015.

B. Konradsen and S. V. Ouren. Modeling the effects of temperature and frequency on bitumen-coated helical cable elements. In *Proceedings of the 55th Conference on Simulation and Modelling (SIMS 2014) - Aalborg, Denmark*, 2014.

E. Kreyszig. *Advanced engineering mathematics - 10th edition*. John Wiley & Sons, Inc., 2011.

P. Maioli. Bending stiffness of submarine cables. In *Proceedings of the 9th International Conference on Insulated Power Cables (Jicable '15)*, 2015.

J. Mullins, D. Morin, A. Tyrberg, C. Sonesson, and J. Ekh. Bitumen shear mechanics in a dynamic subsea electrical cable. In *Proceedings of the ASME 2015 34th International Conference on Ocean, Offshore and Arctic Engineering OMAE 2015*, 2015.

E. Olsen, K. A. Hansen-Zahl, and S. Karlsen. Viscoelastic behaviour of bitumen in dynamic control umbilicals. In *Proceedings of the ASME 33rd International Conference on Ocean, Offshore and Arctic Engineering OMAE 2014*, 2014.

H. See. Advances in measuring linear viscoelastic properties using novel deformation geometries and Fourier transform techniques. *Korea-Australia Rheology Journal*, 13(2):67–81, 2001.

J. Tarnowski. Improved method of determining bending stiffness of underground cables. In *Proceedings of the 9th International Conference on Insulated Power Cables (Jicable '15)*, 2015.

DOI 10.3384/ecp1511943